



This is a repository copy of *Evaluation of copper slag and stainless steel slag as replacements for blast furnace slag in binary and ternary alkali-activated cements*.

White Rose Research Online URL for this paper:

<https://eprints.whiterose.ac.uk/202615/>

Version: Published Version

Article:

Stefanini, L. orcid.org/0000-0002-6871-6879, Ghorbani, S., De Schutter, G. et al. (3 more authors) (2023) Evaluation of copper slag and stainless steel slag as replacements for blast furnace slag in binary and ternary alkali-activated cements. *Journal of Materials Science*, 58 (31). pp. 12537-12558. ISSN 0022-2461

<https://doi.org/10.1007/s10853-023-08815-7>

Reuse

This article is distributed under the terms of the Creative Commons Attribution (CC BY) licence. This licence allows you to distribute, remix, tweak, and build upon the work, even commercially, as long as you credit the authors for the original work. More information and the full terms of the licence here:

<https://creativecommons.org/licenses/>

Takedown

If you consider content in White Rose Research Online to be in breach of UK law, please notify us by emailing eprints@whiterose.ac.uk including the URL of the record and the reason for the withdrawal request.



eprints@whiterose.ac.uk
<https://eprints.whiterose.ac.uk/>



Evaluation of copper slag and stainless steel slag as replacements for blast furnace slag in binary and ternary alkali-activated cements

Laura Stefanini^{1,2} , Saeid Ghorbani³, Geert De Schutter³, Stijn Matthys³, Brant Walkley⁴, and John L. Provis^{1,*} 

¹Department of Materials Science & Engineering, University of Sheffield, Sir Robert Hadfield Building, Mappin Street, Sheffield S1 3JD, UK

²Grantham Centre for Sustainable Futures, University of Sheffield, Sheffield, UK

³Department of Structural Engineering and Building Materials, Faculty of Engineering and Architecture, Magnel-Vandepitte Laboratory, Ghent University, Technologiepark-Zwijnaarde 60, 9052 Ghent, Belgium

⁴Department of Chemical & Biological Engineering, University of Sheffield, Sir Robert Hadfield Building, Mappin Street, Sheffield S1 3JD, UK

Received: 8 June 2023

Accepted: 24 July 2023

Published online:

10 August 2023

© The Author(s) 2023

ABSTRACT

Commonly used alkali activation precursors such as blast furnace slag and fly ash will soon become less available due to resource competition, and may cease to be produced in certain regions. This limitation in future supply is a main driving force for the investigation of alternative precursor sources, such as non-blast furnace slags and non-ferrous slags, to produce alkali-activated binders. The current study investigates the incorporation of copper slag (CS) and stainless steel slag resulting from electric arc furnace operations (EAFSS) as partial replacements for ground granulated blast furnace slag (GGBFS) in producing alkali-activated materials (AAMs), at paste level. Five binary alkali-activated mixtures with different replacement levels of GGBFS with CS, and three ternary mixtures with both CS and EAFSS as partial and total replacements for GGBFS, are activated by a sodium silicate solution. Replacing GGBFS with CS and EAFSS retards the reaction kinetics, resulting in improved fresh-state properties of the investigated AAMs, better retention of workability and longer setting times. The reaction of alkali-activated 100% CS shows minimal initial exothermic activity until 3.5 h, when a single intense peak appears, representing delayed dissolution and subsequent polycondensation. X-ray diffraction (XRD) data indicate that the main crystalline phases of CS and EAFSS are stable in these alkaline systems; it is the glassy components that react. The use of CS and

Handling Editor: M. Grant Norton.

Laura Stefanini and Saeid Ghorbani have contributed equally to this work.

Address correspondence to E-mail: j.provis@sheffield.ac.uk

EAFSS in blended AAMs causes a minor increase in porosity of $\sim 1\text{--}3\%$ with respect to GGBFS only, and a small reduction in compressive and flexural strengths, although these reach 80 MPa and 8 MPa, respectively, after 28 days, even at a replacement level over 65 wt. %. Conversely, the 100% CS mixture exhibits a one-day compressive strength of 23 MPa, with a negligible increase thereafter. This result agrees with both FTIR and SEM analysis which highlight only minor changes in binder development after two days. It is believed that the unusual behaviour of CS in the investigated mixtures is related to the low availability of calcium in this precursor material.

Introduction

Recycling and repurposing of various industrial waste materials and by-products for use in the construction industry have attained increased attention as a means to decrease the negative intrinsic environmental impacts of the industry, whilst providing new economic opportunities [1–4]. These waste materials or by-products predominately consist of minerals that can be processed and treated into secondary raw materials, many of which can potentially be used as supplementary cementitious materials (SCMs) [5, 6]. The construction industry is a heavy emitter of carbon dioxide, with production of Portland cement (PC) alone contributing 5–8% of global emissions [7]. Further emphasis on sustainability has meant that novel low-carbon cements need to be developed as supplementary and alternative technology to PC. One such type of cement with significant potential to lower the overall sector-wide carbon footprint is alkali-activated materials (AAMs) [8–10]. The performance of AAMs is comparable to PC-based systems, with the added benefit of potential property tailoring for specific applications [11, 12]. To produce an AAM, an aluminosilicate source, such as ground granulated blast furnace (GGBFS), metakaolin and/or fly ash, is activated with an aqueous alkaline activator such as sodium hydroxide or sodium silicate [13]. GGBFS and fly ash are the most studied and utilised solid precursors for both AAM and SCM production [14]. This dual use has increased the value of these materials and changed their designation from wastes to secondary resources, with ever-decreasing availability.

Therefore, there now exists a drive to investigate new sources of precursors, such as non-ferrous slags, e.g. copper slag (CS), and non-blast furnace steel slags, e.g. electric arc furnace stainless steel slag

(EAFSS), for the production of AAMs. The global production of CS, a smelting by-product from copper production, is reported to be around 46.20 million tonnes in 2018, with 2.20 tonnes of CS produced for every tonne of copper [15–17]. Steel slags are also generated in considerable volumes, up to about 300–400 kg of slags for each tonne of stainless steel produced [18], with EAFSS being a considerable fraction of this production [19]. EAFSS has applications as a road base material [20, 21], as aggregate in traditional concrete [22] and as a SCM or filler material for Portland cement blends [23]. EAFSS is reported to have a low reactivity, and mainly affects workability and setting times, when used in alkali-activated cements [24–26]. The use of CS as a SCM and an aggregate for PC has been reported in the literature [27–29]; however, there is less published work on its use in the production of AAMs [15, 30–32]. Nazer et al. [31] reported similar compressive strength values to conventional PC mixtures for a hybrid system including 25 wt. % CS as an SCM, after 91 days. Use of sodium silicate as an activator for CS has been reported to be more effective in terms of strength development compared to sodium hydroxide [15, 33]. Curing CS-AAMs at higher temperatures is also noted to improve the reaction rate of the mixtures [34].

Non-ferrous slags often have high iron (> 40 wt. %) and silicon contents, while inclusion of calcium and aluminium is generally limited [35]. The amorphous fraction of these non-ferrous slags can be high, depending on cooling conditions after smelting [36], with iron present in both amorphous and crystalline phases. Crystalline phases containing iron are usually stable in alkaline media and do not participate in the formation of binding phases [37], whereas amorphous iron-rich phases may dissolve and have a pronounced effect on the polycondensation reaction

[38–40]. Other vitreous iron-rich precursors have proved to be suitable for alkali activation including iron silicate glasses from municipal solid wastes [41], low-calcium copper–nickel slags [42] and ferro-nickel slags from electric arc furnaces [43].

The present study investigates the incorporation of CS and EAFSS as partial and total replacements for GGBFS in AAMs. Isothermal calorimetry, setting time and mini-slump tests are conducted to better understand the fresh-state and early hydration properties. The microstructural development of the resulting alkali-activated binders is characterised using X-ray diffraction (XRD), Fourier transform infrared spectroscopy (FTIR), scanning electron microscopy (SEM) and mercury intrusion porosimetry (MIP) techniques. The leaching of heavy metals is also assessed. A hypothesis on the CS inclusions enabling the formation of “iron-rich” binding phases together with well-known C–A–S–H-type gels is proposed.

Materials and methods

GGBFS, CS and EAFSS characterisation

Three types of solid precursors were used: GGBFS (supplied by Ecocem, Belgium; type eco₂cem), CS (supplied by Aurubis Beerse, Belgium; type Koranel 419) and EAFSS (supplied by Orbix; type Fillinox 3000) to produce the AAMs. The particle size distributions of the precursor materials, determined by laser diffraction using Mastersizer 2000 instrument are shown in Fig. 1a. The d_{90} , d_{50} and d_{10} values of the solid precursors derived from the particle size distribution curves are given in Table 1, along with their measured densities. Both GGBFS and CS materials have similar size distributions with centres at ~ 10 – $11 \mu\text{m}$, whilst EAFSS has a bimodal distribution, centred at $\sim 1 \mu\text{m}$ and $\sim 10 \mu\text{m}$.

Table 1 also shows the chemical compositions of the solid precursors identified using X-ray fluorescence spectroscopy (XRF). The main difference between GGBFS and EAFSS is the disparity in concentrations of Al_2O_3 , MgO and SO_3 . The EAFSS used here also contains a high concentration of chromium, well above that which is expected in conventional stainless steel slags [44]. The CS composition is characterised by low CaO content and high Fe_2O_3 content compared to GGBFS and EAFSS.

Inspection of CS and EAFSS particles via SEM (Fig. 1b to d) shows more regular morphologies compared to the angular shape of GGBFS particles.

Figure 2a shows the X-ray diffraction (XRD) patterns of the raw materials. GGBFS and CS are predominantly amorphous, exhibiting a distinctive hump at $\sim 30^\circ 2\theta$. This hump for CS is broader and is slightly shifted to higher 2θ . Minor crystalline phases are also present, identified as cubic fayalite (Fe_2SiO_4 , PDF #04–017–9804) and orthorhombic fayalite (PDF #00–034–0178), hematite (Fe_2O_3 , PDF #00–056–1302) and ankerite ($\text{Ca}(\text{Fe},\text{Mg},\text{Mn})(\text{CO}_3)_2$, PDF #00–033–0282). The mineral composition defined here is in agreement with several previous studies [3, 15, 16, 45]. The major crystalline phases of EAFSS are from the melilite group, mainly åkermanite ($\text{Ca}_2\text{MgSi}_2\text{O}_7$) with a partial aluminium replacement (åkermanite aluminian, $\text{Ca}_2\text{Mg}_{0.9}\text{Al}_{0.2}\text{Si}_{1.9}\text{O}_7$, PDF# 04–014–4688), and merwinite ($\text{Ca}_3\text{Mg}(\text{SiO}_4)_2$, PDF# 01–086–6219). Minor phases are identified as a mixed spinel phase ($\text{Fe},\text{Mg},\text{Al})\text{Cr}_2\text{O}_4$ (PDF# 04–016–2691), calcite (CaCO_3 , PDF# 01–086–4272), wollastonite (CaSiO_3 , PDF# 00–027–0088) and traces of free lime (CaO , PDF# 00–037–1497). This EAFSS phase assemblage is consistent with previous studies, albeit highly dependent on the cooling conditions, initial composition and type of initial scrap used in the EAF, which necessitates a case by case study of slag precursors from differing sources. When compared with values presented in the literature, the EAFSS used in this study has a particularly high chromium content and low iron content [16, 44, 46].

Figure 2b displays the FTIR spectra of the precursor materials. The GGBFS spectrum shows two major absorption bands between 1000 and 900 cm^{-1} and at $\sim 500 \text{ cm}^{-1}$ corresponding to Si–O–T (T = tetrahedral Si or Al) asymmetric stretching vibrations and Si–O asymmetric bending vibrations, respectively. Similar absorption bands at 970 – 920 cm^{-1} and at $\sim 500 \text{ cm}^{-1}$ are identified in the CS spectrum; in this case the asymmetric stretching vibrations Si–O–T could involve T = Si, Al and/or Fe^{3+} [47]. The broadness and smoothness of these peaks indicate a highly amorphous structure consisting predominantly of silicates [48]. The sharper peaks in the CS spectrum at $\sim 947 \text{ cm}^{-1}$ correspond to the vibrational modes of crystalline fayalite [49]. The GGBFS spectrum shows an additional signal at $\sim 700 \text{ cm}^{-1}$, related to symmetric Si–O–Si bond stretching, that is not clearly identified in the CS spectrum. The

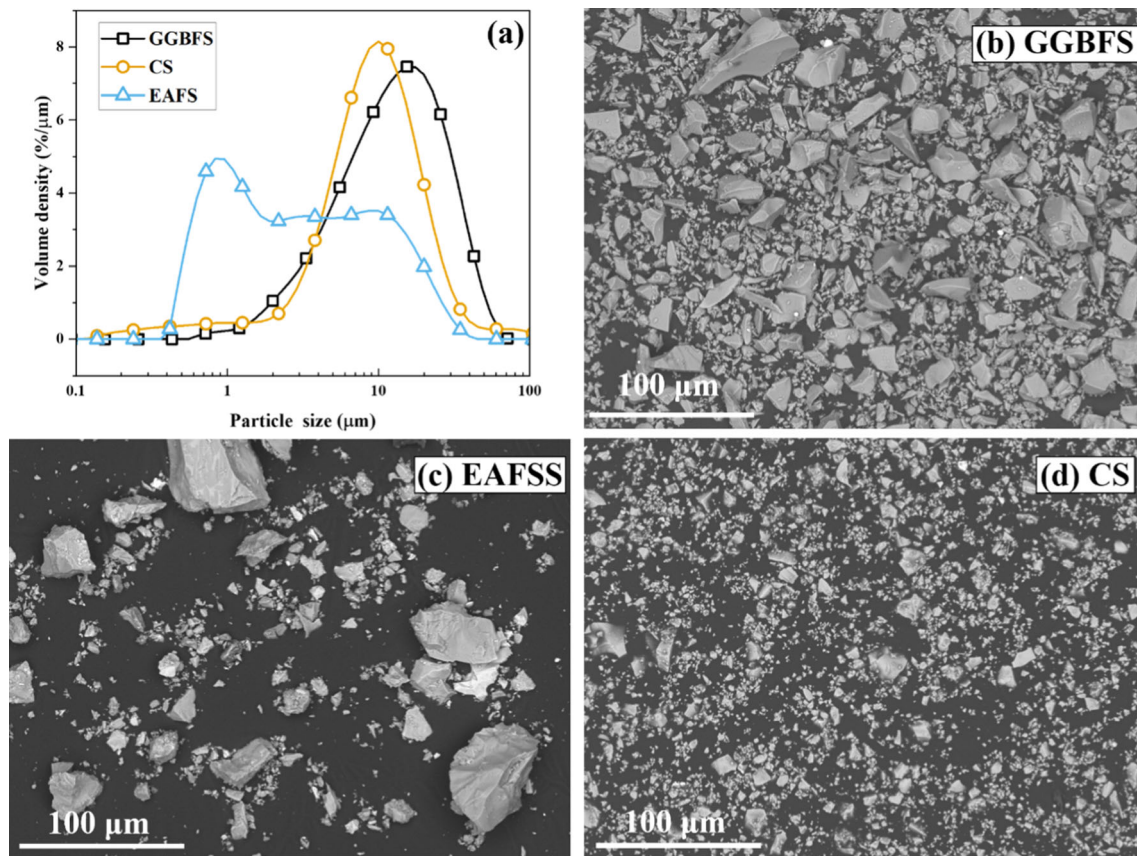


Figure 1 a Particle size distributions of GGBFS, CS and EAFSS; morphology of solid precursors as observed by SEM: b GGBFS, c EAFSS and d CS.

Table 1 Physical properties and chemical compositions of GGBFS, CS and EAFSS

Solid precursor	Density g/cm ³	Particle size distribution (μm)			Chemical composition (wt. %)												
		d ₉₀	d ₅₀	d ₁₀	SiO ₂	CaO	Al ₂ O ₃	Fe ₂ O ₃	MgO	SO ₃	K ₂ O	MnO	Cr ₂ O ₃	Na ₂ O	ZnO	Others	
GGBFS	2.89	23.5	8.0	1.4	31.1	40.9	13.7	0.4	9.2	2.3	0.7	0.3	–	–	–	1.4	
CS	3.45	22.8	9.9	3.2	29.5	2.6	9.9	45.4	1.0	0.9	0.2	0.7	1.4	3.4	3.3	1.7	
EAFSS	3.25	15.6	3.0	0.8	28.0	44.2	6.3	2.0	4.4	0.5	0.1	2.7	9.9	–	–	1.9	

maximum of the Si–O–T band is located at 970 cm⁻¹ for GGBFS and at 947 cm⁻¹ for CS. This shift towards lower wave numbers is indicative of an amorphous network with more highly substituted silicon tetrahedra (due to the high Fe³⁺ content) [50]. The EAFSS spectrum similarly exhibits these two main bands, between 1000 and 900 cm⁻¹ and at ~ 500 cm⁻¹, corroborating that silicates (calcium silicates with Mg and Al) are the most abundant phases as shown in

the XRD in Fig. 2a. Beside these bands, several well-defined and sharp peaks are detected for the crystalline phases present. Peaks at 1425 cm⁻¹, 875 cm⁻¹ and 713 cm⁻¹ are attributed to calcite, specifically the C–O asymmetric stretching vibration and C–O out-of-plane and in-plane bending [51]. The bands at 637 cm⁻¹ and the shoulder at 500 cm⁻¹ are due to the Cr(III)-O vibration characteristic of the spinel phase (Fe, Mg, Al)Cr₂O₄ [52]. The remnant peaks at 1018

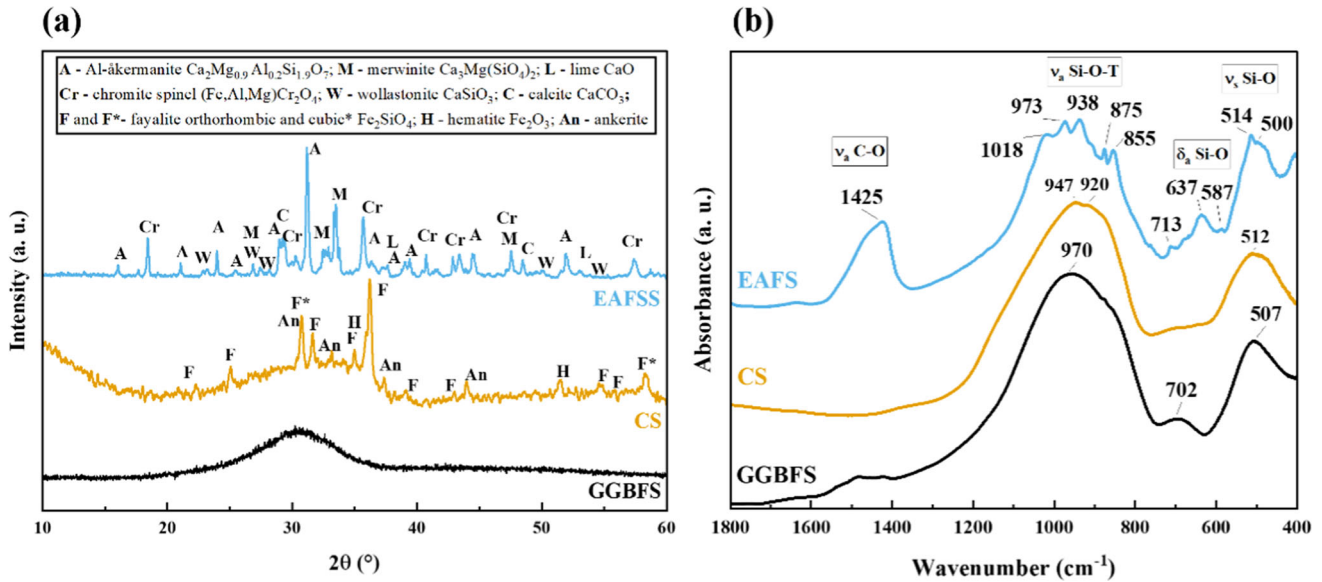


Figure 2 a X-ray diffraction patterns and b FTIR spectra of the precursors GGBFS, CS and EAFSS.

cm^{-1} , 973 cm^{-1} , 938 cm^{-1} , 855 cm^{-1} and 587 cm^{-1} are associated with the presence of crystalline åkermanite, merwinite and wollastonite [53].

Activator solution and sand

Sodium hydroxide pellets (purity of 98%, provided by Sigma-Aldrich), and sodium silicate (type CRYSTAL 0112, provided by PQ Corporation) with original $\text{SiO}_2/\text{Na}_2\text{O}$ ratio of 2, were used as activators. Standard CEN sand (Normesand, Germany) according to EN 196 [54] was used as a fine aggregate to produce the mortar mixtures in this study.

Specimen preparation

The solid precursors (GGBFS, CS and EAFSS) were initially dry-mixed for 60 s in a Hobart mixer to homogenise, then sand was added and blended for 60 s into the pre-mixed powders to prepare mortars. The alkali solution was prepared 24 h prior mixing, made of sodium hydroxide, sodium silicate and water to give a molar ratio ($\text{SiO}_2/\text{Na}_2\text{O}$) = 1.6, an activator dosage of 5.3 wt. % (defined as Na_2O wt. % with respect to wt. of solid precursors GGBFS + CS + EAFSS) and a water binder mass ratio (w/b) = 0.32, with the solution kept constant for all AAMs. The precursors and alkaline solution were mixed for 60 s at low speed (140 rpm), then for 90 s at high speed (285 rpm) to achieve a homogeneous

mixture. The preparation of pastes followed the same procedure, except for the sand addition. A total of eight AAMs with different replacement levels of GGBFS were produced: five binary mixtures with CS replacement levels of 0, 25, 50, 75 and 100 wt.%, three ternary mixtures with 50 wt.% CS and EAFSS inclusions at 15, 25 and 35 wt.%. The mix proportions of all mixtures, each of which was prepared as paste and mortar specimens, are shown in Table 2.

Testing programme

Isothermal calorimetry

The reaction kinetics of alkali-activated pastes were investigated by isothermal calorimetry using a TAM Air Conduction Calorimeter (TA Instruments, USA). To prepare the mixtures according to the mix proportions given in Table 2, 10 g of solid precursors were weighed, transferred into a glass vial and dry-mixed. The alkaline solution was added using a pipette and manually mixed for ~ 30 s. The vial was sealed and promptly loaded into the calorimeter along with a reference vial filled with water, as described by Wadsö [55]. The heat evolution was recorded for 150 h. The results are presented as heat release per gram of solid binder, i.e. the sum of the mass of the precursor and the solid constituents of the activators.

Table 2 Mix proportions

Mixture	Precursors (g)			Activator solution (g)			w/b mass ratio	Sand in mortars (g)
	GGBFS	CS	EAFSS	Sodium silicate	NaOH	Water		
100G	560.0	0	0	160.0	7.7	117.5	0.32	1535.0
25C	420.0	140.0	0	160.0	7.7	117.5	0.32	1535.0
50C	280.0	280.0	0	160.0	7.7	117.5	0.32	1535.0
75C	140.0	420.0	0	160.0	7.7	117.5	0.32	1535.0
50C/15E	196.0	280.0	84.0	160.0	7.7	117.5	0.32	1535.0
50C/25E	140.0	280.0	140.0	160.0	7.7	117.5	0.32	1535.0
50C/35E	84.0	280.0	196.0	160.0	7.7	117.5	0.32	1535.0
100C	0	0	560.0	160.0	7.7	117.5	0.32	1535.0

Mini-slump test and setting time

To assess the workability of pastes over time, a mini-slump test was performed at three different time intervals: 5, 30 and 60 min from the beginning of mixing. A slump cone with a height of 40 mm, internal top and bottom diameters of 38 and 60 mm, respectively, was used. At each target testing time, the AAM pastes were manually remixed for 60 s before the test. For each slump test, the slump cone was placed on a flat sheet and gradually filled with the fresh AAM paste mixture. The cone was then lifted as slowly as possible (< 1 cm/s) [56], and the mean value of the flow diameters in two perpendicular directions was recorded as the spread value.

The Vicat technique was used to evaluate initial and final setting times of fresh alkali-activated pastes. Experimentals were performed in an automatic Matest VICATRONIC apparatus (Impact Test Equipment, UK) equipped with a 1.13 mm needle following, as closely as possible for these materials, the standard testing procedure EN 196–3 [54]. Fresh pastes were poured into a conical frustum mould with a height of 40 mm, top internal diameter of 60 mm and bottom internal diameter of 70 mm. The initial setting time was determined as the time at which the separation between the needle and the base plate first reached 6 ± 3 mm. The final setting time was recorded once a maximum penetration depth of 0.5 mm into the specimen was reached.

X-ray diffraction

XRD analysis was performed using a PANalytical X'Pert³ phase instrument fitted with a one-

dimensional PIXcel-Medipix3 detector, in the Bragg–Brentano geometry, with a step size of 0.02° and a 2θ range from 5° to 60° using a Cu X-ray source running at 45 kV and 40 mA. Qualitative phase identification was carried out using PDF + 4 (ICDD, USA) and HighScore plus (Malvern Panalytical, UK).

Fourier transform infrared spectroscopy

Fourier transform infrared spectroscopy (FTIR) analysis was performed using a PerkinElmer Frontier FTIR spectrometer (PerkinElmer, USA) coupled with a triglycine sulphate detector. A sample of 2 mg of precursor material was mixed and ground together with 200 mg of KBr. The mixed powder was transferred to a 13 mm pellet die and pressed at 700 MPa to form a transparent pellet. FTIR spectra were collected as an average of 32 scans between 4000 and 400 cm^{-1} , with a resolution of 0.25 cm^{-1} .

Scanning electron microscopy

Scanning electron microscopy (SEM) was conducted using a Hitachi TM3030 coupled with the EDS (energy-dispersive X-ray spectroscopy) software Bruker QUANTAX 70. Powder specimens were prepared by placing a small amount of powder material on a carbon dot adhered to a 12.5 mm aluminium SEM pin stub. Loose powder was removed using compressed air. Hardened paste fragments were mounted in epoxy resin, left to cure overnight and demoulded ready for polishing. Samples were polished using SiC sandpaper in ascending grits and carbon-coated prior to SEM analysis.

Mercury intrusion porosimetry

Mercury intrusion porosimetry (MIP) tests were carried out to study the pore structure of the paste specimens within the range of 6.5 nm–100 μm after 2 and 28 days. Tested samples consisted of approximately 1.5 g of fractured particles with random morphologies. Prior to MIP measurements, the collected pieces were exposed to isopropanol for a day to arrest the polycondensation reaction. The pieces were then dried in an oven at 35 °C until reaching a constant mass. After oven-drying, the pieces were further vacuum-dried at 20 ± 2 °C for one week at 0.1 bar.

MIP measurements were performed using both Pascal 140 (low-pressure) and 440 (high-pressure) mercury porosimeters (Thermo Scientific). The maximum pressure was limited to 200 MPa during the measurements to avoid sample cracking due to the mercury pressure. The contact angle between the mercury and the solid surface was assumed to be 130° [57].

Strength properties

The compressive and flexural strengths of mortar mixtures were determined at different curing ages (1, 3, 7 and 28 days) on 40 × 40 × 160 mm specimens according to EN 1015–11 [58]. Fresh mortar mixtures were poured into moulds and subsequently demoulded 24 h after casting. Samples were sealed with plastic film and stored in a curing chamber with a fixed relative humidity of 95% at 20 ± 0.1 °C until testing. The strength values for the mixtures at every testing day are reported as the mean value of six compressive and three flexural tensile tests, respectively.

Leaching test methodology

The leaching of heavy metals for paste monoliths was studied for a period of 91 days immersed in water following the procedure described in NEN-7345:94 [59] (tank test). Three cylindrical paste monoliths

were prepared for every composition, each with a diameter of 10 mm and height of 50 mm. Samples were cured for 28 days under sealed conditions and then immersed into distilled water in a closed vessel with a liquid/solid volume ratio of 5. Prior to immersion, both bases of the monoliths were covered with epoxy resin to avoid contact with water. Extractions of leachate occurred after 1 h, 24 h, then 3, 7, 14, 28, 56 and 91 days for each sample. Each leachate was passed through 0.2 μm filter paper and sent for ICP analysis to an external laboratory.

The fraction of leachate (E_i) is calculated as:

$$E_i = \frac{C_i \cdot V}{A} \tag{1}$$

where C_i is the concentration of the component in fraction i , V is the volume of the eluate and A is the exposed surface area of the specimen, which in this case is the lateral surface area of the cylinder monoliths only.

The cumulative leaching value is then calculated for each component as:

$$\varepsilon_n = \sum_{i=1}^N E_i \tag{2}$$

for each of the n elements of potential concern, where N is the number of extractions ($N = 8$ in this case).

The materials are classified as a function of cumulative leaching value for each leachate in three following categories according to the limiting concentrations U1 and U2 as shown in Table 3:

Category 1 (C1): ε_n is lower than U1 for each heavy metal present in the sample. These materials do not present any environmental restriction in their use.

Category 2 (C2): ε_n is between U1 and U2 for some of the heavy metals present in the sample, but not exceeding U2 for any element. These materials do not face any environmental restriction in their use, but after their service life it is compulsory to remove the contaminant elements with concentrations higher than U1.

Category 3 (C3): ε_n is higher than U2 for one or more elements. These materials have a limited utilisation.

Table 3 Heavy metal leaching limits (U1 and U2) established by NEN-7345:94 [59]

	As	Ba	Cd	Co	Cr	Cu	Hg	Mo	Ni	Pb	Sb	Se	V	Zn
U1 (mg/m ²)	40	600	1	25	150	50	0.4	15	50	100	3.5	3	250	200
U2 (mg/m ²)	300	45,000	7.5	200	950	350	3	95	350	800	25	20	1500	1500

Table 3 shows the values of U1 and U2 for selected relevant elements, according to NEN-7345 [59].

Results and discussion

Isothermal calorimetry

The isothermal calorimetry results for the alkali-activated pastes are shown in Figs. 3 and 4. The first exothermic peak present for all samples except 100C occurs within the first 3 h of reaction (Fig. 3I). This initial stage is associated with the wetting and dissolution of solid precursor particles and formation of primary C–A–S–H-type gels [60, 61]. The 100G sample exhibits the highest intensity for this peak. Specimens with CS inclusion show a decreasing trend in dissolution peak intensity and increasing time delay to its onset. Samples 75C and 50C/25E have similar dissolution peak intensities; however, the ternary sample has a delay in peak appearance and a convoluted shape composed of an initial shoulder peak merging into a dissolution peak, with a maximum after 1.5 h. Similar behaviour is seen for 50C/35E, which suggests that the origin of the convoluted dissolution peak is due to the differing dissolution rates of GGBFS and EAFSS particles in alkaline media, with both of these types of slag showing a notable contribution to the reaction process at early age.

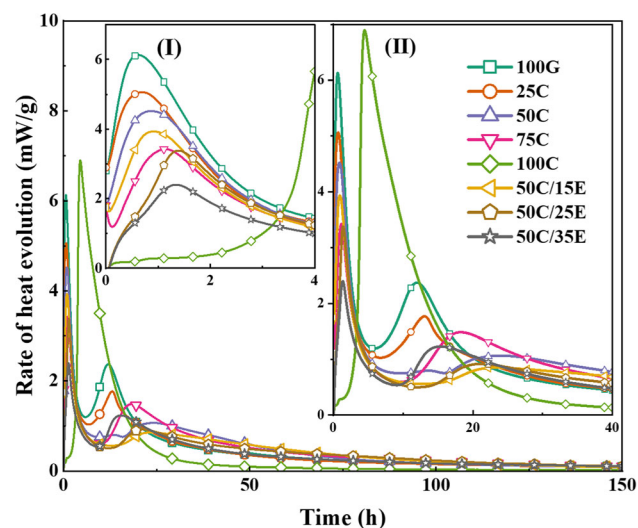


Figure 3 Heat evolution of alkali-activated mixtures based on GGBFS, CS and EAFSS at 20 °C.

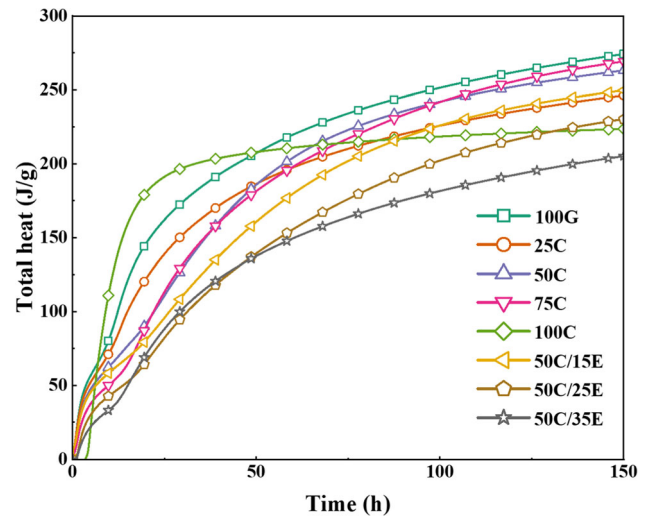


Figure 4 Cumulative heat released by alkali-activated pastes based on GGBFS, CS and EAFSS at 20 °C.

The dissolution peak is followed by a dormant period during which heat release is reduced to a steady state with continuing dissolution [60, 62]. The dormant period is followed by a second exothermic peak Fig. 3II which can be fundamentally divided into two segments: acceleration and deceleration. The heat flow signals in both of these segments can also be convoluted in blended binders, resulting in significant peak broadening due to overlapping contributions from individual precursors and their reaction products. The acceleration period is associated with the primary C–A–S–H undergoing precipitation and polymerisation to form a gel structure, while the deceleration period is linked with further gel densification and hardening, and continues until reaching the steady state. This second peak is the most intense in the 100G sample. By comparison, 25C exhibited a delay of 1.3 h and a 25.7% reduction in maximum heat flow. Larger GGBFS replacements show a similar reduction in maximum intensity accompanied by peak broadening. Sample 100C is the exception, exhibiting a delay in dissolution, with no evidence of exothermic activity during the first 3 h. After 3–4 h, there are a steep acceleration in the heat release profile of 100C, forming a broad singular peak with a maximum after 4.8 h, and a subsequent deceleration period concluding between 20 and 30 h.

The relatively large peak intensity and delayed onset time in CS-blended binders suggests a distinctly different exothermic behaviour due to the dissolution and reaction of iron species. Samples with

both GGBFS and CS would be expected to have combined calorimetry profiles that consist of both the dissolution and reaction of GGBFS and CS, and any interaction effects between the two materials. This is highlighted in the 50C mixtures, showing two delayed secondary signals with lower intensity than the 75C mixture, which does not follow the trend based on the higher GGBFS content mixture. The reaction peak in the 75C mixture occurs after a shorter period of time, indicating that CS now dominates the exothermic behaviour, acting to increase the reaction rate. Both 50C and 50C/15E have convoluted signals in which two peaks are distinguishable, indicating that more than one type of exothermic process is taking place. This may be either a delayed dissolution of CS followed by a more conventional polycondensation reaction or the formation of two distinct gel structures throughout the bulk arising from different gel forming species, i.e. Ca, Si, Al from GGBFS and Fe, Si, Al from CS. The second peak intensity increases, narrows and appears earlier in time with further additions of EAFSS. This behaviour is unusual for low-reactivity precursor materials and may be explained by the high amount of activator available for the reaction of CS due to the limited content of GGBFS in the systems, rapidly forming gel phases. The subsequent deceleration period is clearly reduced, resulting in quick reaction propagation and hardening of the mixtures. Figure 4 shows the total cumulative heat profiles of all samples.

Two distinct effects can be seen when comparing the data of the single precursor mixtures (100G and 100C). The 100C mixture evolves the greatest amount of heat within the first 20 h of reaction followed by a complete cessation of activity thereafter. The 100G mixture shows lower heat evolution after 20 h and, however, continues to react up to the monitored 150 h, resulting in a greater overall magnitude of heat evolution than the 100C system. Unexpectedly, the addition of a small amount of GGBFS to a predominantly CS system (75C) results in the suppression of early-age heat evolution, with continued reactivity seen at later ages, similar to 100G. This could be explained by the GGBFS providing the necessary calcium source for the protracted creation and improvement of the binding phase present in iron silicate systems [40]. Further additions of calcium-

rich material decrease the cumulative rate of heat released at 150 h, suggesting the existence of an optimum in the elemental ratios of the precursors. The inclusion of EAFSS into the mixtures manifests mainly as a filler-type effect.

Mini-slump test and setting time

Figure 5 illustrates the mini-slump test values obtained up to 1 h after mixing, and Vicat initial and final setting time results, for all of the alkali-activated pastes investigated. As shown in Fig. 5a, the solely GGBFS-based mixture has the lowest initial slump flow diameter of 149 mm. All mixtures with CS or EAFSS replacements achieve a slump diameter between 153 and 185 mm. Additions of both CS and EAFSS into GGBFS-based binders have been reported in previous studies to increase the mixture slump [25, 63] despite their small particle sizes (Fig. 1a).

The general trend in slump values shows an increase with CS inclusion, when CS is replaced with EAFSS, as seen for 50C25E. This is a result of the slow dissolution of CS and low early-stage reactivity, as corroborated by the isothermal calorimetry data in Fig. 5 where the first exothermic peak occurs after ~ 4 h. Early reactivity of EAFSS is even lower due to the large fraction of unreactive minerals present, as shown in Fig. 2. Lower angularity of CS and EAFSS particles and higher specific density may also increase the slump diameter, considering the higher apparent liquid-to-solid volume ratio.

After 30 min, the slump values for 100G and 25C mixtures are reduced to a near zero-slump condition, maintaining the cone shape once the mould is removed, suggesting a high early reactivity. For replacement levels of 50 and 65% (50C and 50C15E) the slump loss is less rapid, but these mixes also reach a zero-slump state at 60 min. For further replacement (75C, 50C25E and 50C35E) the slump diameter values remain nearly constant during the initial 30 min and decrease only slightly after 1 h. The slump diameter of 100C does not appear to decrease during the first hour of reaction, indicating very low early reactivity.

Setting times are reported in Fig. 5b. Sample 100G begins to set after 60 min and the completely sets after 70 min, which is considered quick setting. This can be attributed to the high dosage and alkalinity of

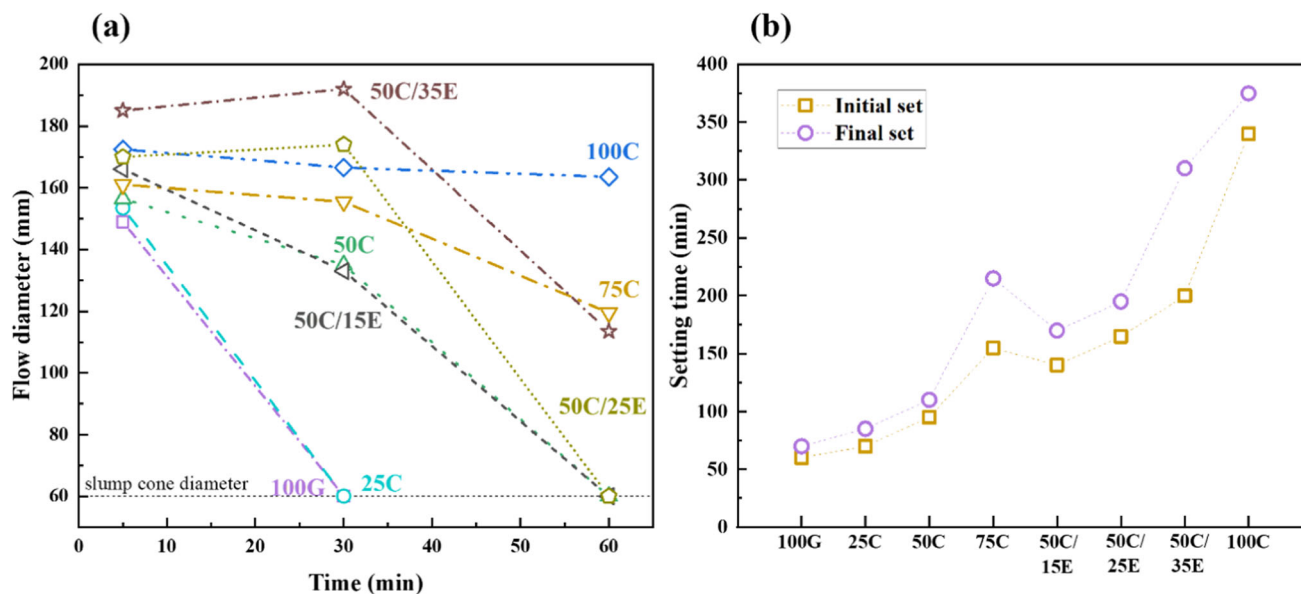


Figure 5 a Mini-slump test and b setting times results for all alkali-activated pastes based on GGBFS, CS and EAFSS.

the activator solution used in this work. Previous studies have demonstrated that the type and the molar ratio of the activator solution are the main factors that affect the setting time of an alkali-activated cement [64]. All initial setting times for binary and ternary mixtures vary between 70 and 200 min, and final setting times between 85 and 310 min. The progressive inclusion of CS and EAFSS results in an increase in the setting time; however, sample 75C has a similar initial setting time but a longer setting period than 50C/25E. A divergence in setting period is also seen for 50C/35E. The 100C mixture is the exception, with the setting process starting after 340 min (5.7 h) with a relatively short setting period of 35 min. Overall the setting periods of the binders here are relatively short, indicating the possibility for rapid development of hardened material properties once the point of initial setting has been reached; this is considered a desirable attribute.

A comparison between setting times and heat evolution calorimetric profiles for 100G and 100C mixtures is shown in Fig. 6. It can be seen that the setting process starts shortly after the beginning of the deceleration stage of the dissolution peak for 100G. Similarly, for alkali-activated CS the setting process can be seen to coincide with the single peak in the calorimetric profile. The acceleration period may be associated with the delayed dissolution of CS particles. The setting process starts 1 h after the beginning of the deceleration stage, indicating that

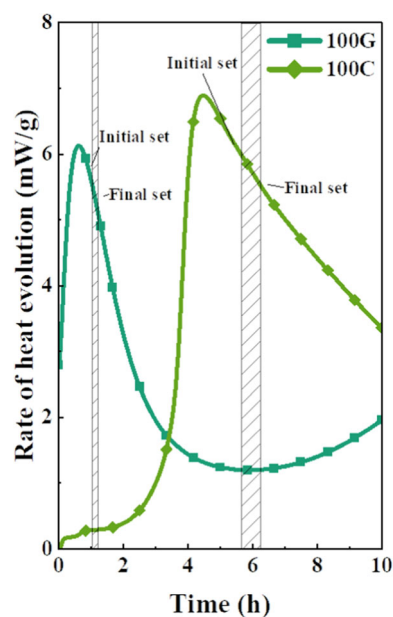


Figure 6 Comparison of setting times and heat evolution profiles for samples 100G and 100C.

dissolution, setting, and gel formation and propagation take place sequentially.

X-ray diffraction

Figure 7 shows the XRD patterns for 100G, 50C, 50G/15E and 100C mixtures obtained after 2 and 28 days of curing.

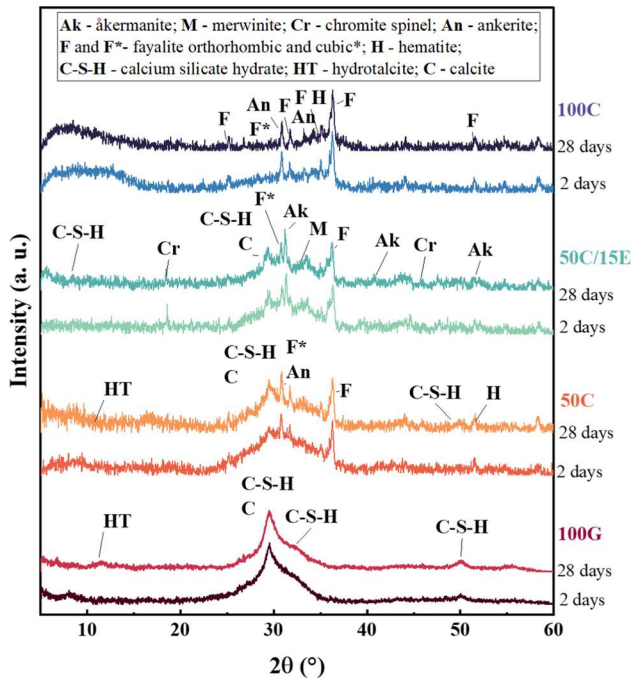


Figure 7 XRD patterns of alkali-activated pastes based on GGBFS, CS and EAFSS after 2 and 28 days.

The pattern for alkali-activated GGBFS (100G) shows distinct diffuse peaks (also called “amorphous humps”), at 29, 33 and 50° 2θ, indicative of C–A–S–H gel formation [65]. The only crystalline feature seen above the first diffuse peak at ~ 29° 2θ is identified as calcite, which is a common surface carbonation product. The main time-dependent phase evolution concerns the degree of C–A–S–H formation, with a narrowing of the diffuse peak indicating increased short range ordering, reflecting a higher degree of polymerisation of the gel phase [66]. The presence of hydrotalcite-type phases (HT, approximately $Mg_4Al_2(CO_3)(OH)_{12} \cdot 3H_2O$ resembling the mineral quin-tinite, PDF#01–089-0460), which are expected to form from the dissolution of the large Mg component of GGBFS [67, 68], are not detected in the XRD patterns for specimens cured for less than 28 days. The appearance of a hump at ~ 12° in the 100G specimen demonstrates low levels of HT formation that can be detected only at 28 days. The broad peak suggests only very small (nanoscale) ordered crystallites of HT-type phases are present [68, 69]. Such slow growth of ordered HT-type structures is attributed to the use of high-molar-ratio activators (high Si content) which readily form concentrated regions of C–A–S–H-type gels hindering any further mobility of

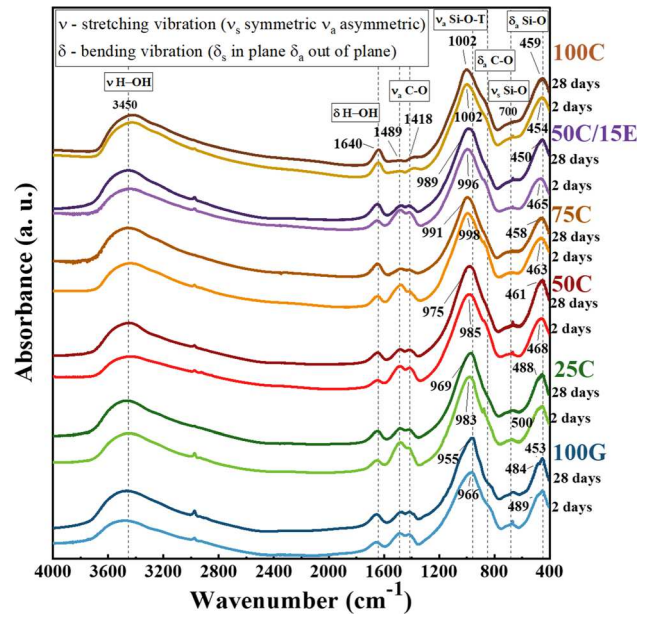


Figure 8 FTIR spectra of AAMs based on GGBFS, CS and EAFSS after 2 days and 28 days.

readily dissolved species, in this case Al, necessary for HT formation.

XRD patterns for 50C show similar trends of calcite and C–A–S–H gel formation, but the further development of these phases is limited after 2 days, and significant HT is not clearly identified at 28 days. Identification of the narrow intense peaks, originating from the inclusion of CS, found satisfactory agreement with references for the minerals fayalite, ankerite and hematite. It is believed that these crystalline phases remain stable and do not contribute to the formation of binding phases [70, 71]. The ternary binder 50C/15E, as well as containing the main minerals of CS, also includes the crystalline phases present in EAFSS: åkermanite, merwinite and chromite spinel as discussed above, whereas HT is not identified due to the limited content of GGBFS in the mixture. EAFSS phases also have very low reactivity in alkaline media [25]. Further increasing CS addition results in a suppression in the intensity of the C–A–S–H hump, indicating a pronounced effect on the overall quantity of C–A–S–H gel formation. This decrease in C–A–S–H gel formation can be attributed to the decrease in readily available Ca within the system, as is noted in the 100C mixture.

Fourier transform infrared spectroscopy

The FTIR spectra were recorded for all mixtures after 2 and 28 days of curing, as presented in Fig. 8.

The main bands exhibited after alkali activation are at $\sim 3450\text{ cm}^{-1}$ and 1640 cm^{-1} , attributed to O–H stretching vibrations and H–O–H bending vibrations, respectively. These bands are characteristic of weakly adsorbed water molecules captured in remnant bulk porosity or on the surface of the alkali-activated samples and can be associated with the presence of products of hydration, i.e. C–A–S–H-type gels [48, 72]. The peaks at 1489 cm^{-1} and 1418 cm^{-1} correspond to the stretching vibration of O=C=O bonds of the carbonate group (CO_3^{2-}) for poorly crystalline vaterite, aragonite and/or calcite [73, 74]; calcite was initially present only in EAFSS (Fig. 2c). The appearance of these bands for partially ordered carbonates is due to the reaction between atmospheric carbon dioxide and the surface of the binders. The contribution of carbonation is larger at early ages (2 days of curing), with decreasing band intensity after 28 days. The suppression of these bands in the 100C sample can be explained by the very low calcium content present, allowing for only limited carbonation to occur. The main band located at $1200\text{--}800\text{ cm}^{-1}$ (asymmetric stretching vibrations of Si–O–T (T = Si, Al, Fe) bonds) is associated with the degree of polycondensation and resulting formation of silicate gels [75–77]. This band for the 100G mixture shows a shift to lower wave numbers with respect to the solid precursors, from 970 cm^{-1} to 966 cm^{-1} after 2 days and to 955 cm^{-1} after 28 days. This trend is reported in the literature to arise from the increased incorporation of Al species and consequently an increased contribution from Al–O–Si linkages [66]. This peak becomes distinctively narrower and sharper with increasing the curing time, which indicates an increasing degree of polycondensation [66]. Conversely, all other mixtures show a shift towards higher wave numbers with respect to both the precursors, in accordance with the previous literature on CS behaviour [32, 40, 49, 78]. This is due to the combined effect of increasing silicate content in the gel and may also related to the oxidation of iron present in the CS from Fe^{2+} to Fe^{3+} [78, 79].

For increasing CS replacement (25C, 50C and 75C), the curing time decreases the magnitude of the band shift; between 2 and 28 days the gap is reduced from 983 cm^{-1} to 969 cm^{-1} for 25C, from 985 cm^{-1} to

975 cm^{-1} for 50C, and from 998 cm^{-1} to 991 cm^{-1} for 75C as the incorporation of Al^{3+} or Fe^{3+} into the gel proceeds. This shift is accompanied by a narrowing/sharpening of the band for 25C mixture, suggesting a higher degree of polymerisation in the gel, whilst a less marked impact can be observed for 50C and 75C mixtures. For the 50C15E specimen, the Si–O stretching vibration also moves towards lower wave numbers (996 cm^{-1} to 989 cm^{-1}), similarly to 75C, whereas the stretching band for the 100C mixture has already reached its final wave number after 2 days of curing with no apparent shift seen between 2 and 28 days. This suggests a very low rate of ongoing reaction in 100C, with the broad Si–O stretching band centred around 1002 cm^{-1} , in agreement with the calorimetric data (Sect. “Isothermal calorimetry”) highlighting activity before 48 h reaching a steady state, with no subsequent strength development noted after the one-day test. The Si–O bending band, at $500\text{--}512\text{ cm}^{-1}$, shifts towards lower wave numbers with respect to the precursors (Fig. 2b) after alkali activation for all samples, further indicating the AAM network developing through Al and Fe incorporation [80].

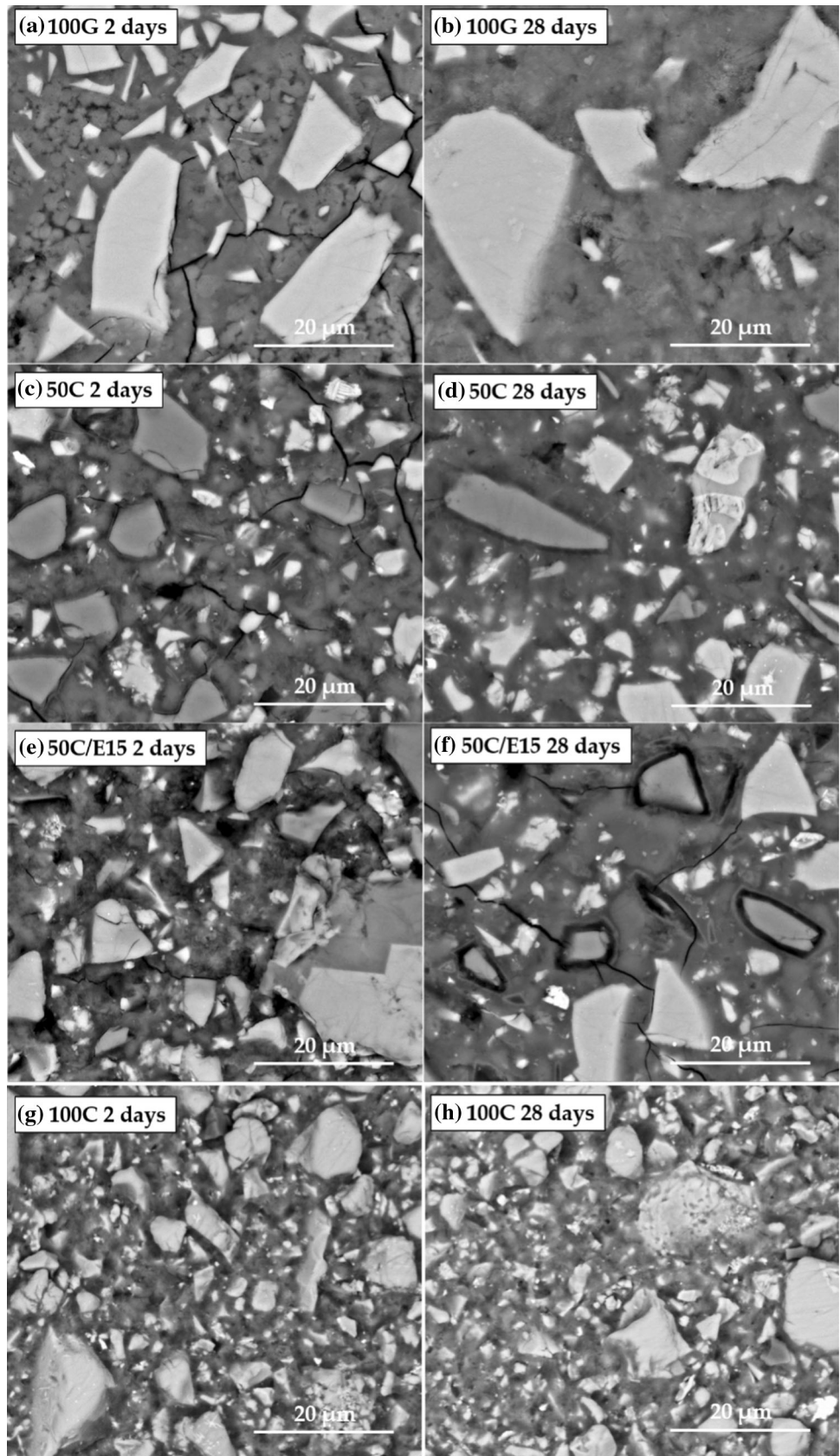
Scanning electron microscopy

Backscattered electron (BSE) images of alkali-activated pastes at 2 and 28 days of curing are displayed in Fig. 9.

Several distinctive microstructural features are seen in the 100G 2-day sample (Fig. 9a), including large unreacted and/or partially reacted GGBFS particles (light grey) surrounded by a heterogeneous matrix of smaller dissolving GGBFS particles, an initial binder phase (grey) and darker regions identified as porosity. The 100G 28-day specimen (Fig. 9b) consists of a highly homogenous dense matrix resulting from the further dissolution of small GGBFS particles and a consequently increased fraction of binding phase present. Large unreacted GGBFS particles persist throughout the matrix.

In the 50C 2-day sample (Fig. 9c), we can identify large GGBFS particles and CS particles (white) surrounded by a heterogeneous matrix. There is a clear difference in particle size distribution between the residual GGBFS and CS, linked in part to the high reactivity of small GGBFS particles in forming the initial matrix phase. The contribution of the CS seems to be limited, by comparison of the 2-day and 28-day

Figure 9 Backscattered electron images of samples 100G, 50C, 50C/15E and 100C after 2 and 28 days of curing.



microstructures. The 50C 28-day microstructure (Fig. 9d) shows progressive densification, generating a more compact and homogenous binder with remnant unreacted GGBFS and CS particles. 50C/15E, in addition to the GGBFS and CS particles, also contains large residual particles of EAFSS.

The structural evolution and the increase in the matrix gel fraction are also considerable when comparing 50C/15E at 2 and 28 days in Fig. 9e and f; however, some newly formed macropores are noted within the binder after 28 days along with some induced microcracks. Even though the porosity is on a much larger length scale, beyond the scope of MIP analysis (see Sect. 1.6), the effect can be attributed to the high content of stable minerals. The differences between 2-day and 28-day 100C microstructures (Fig. 9g and h) appears to be minimal. There exists a binding phase, albeit much lower in extent than the specimens with GGBFS, surrounded by unreacted CS particles. The lack of microstructural evolution regarding the dissolution of CS particles between 2 and 28 days agrees with all data presented.

Evolutions in the chemical composition of alkali-activated specimens 100G, 50C and 100C with increasing curing time from 2 to 28 days as analysed by SEM–EDX are reported in Fig. 10, along with the elemental composition of precursor materials, GGBFS and CS. For each sample, ten EDS points are selected in homogeneous region of the bulk to be

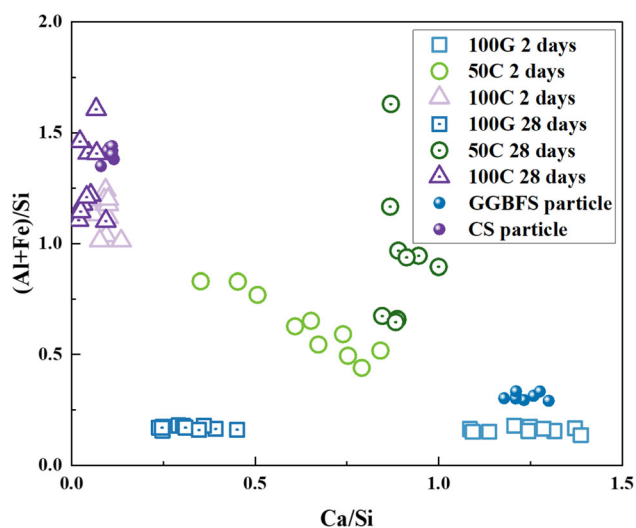


Figure 10 Plot of $(Al + Fe)/Si$ vs Ca/Si mass ratios obtained from EDX analysis of distinctive matrix regions for samples 100G, 50C and 100C after 2 and 28 days, along with precursor materials, GGBFS and CS.

representative of the gel. The Ca/Si versus $(Al + Fe)/Si$ atomic ratio is identified for each point. 100G after 2 days has Ca/Si ratio in the same range as the raw GGBFS whilst the Al/Si ratio ($Fe \sim 0$ in this sample) is slightly inferior as should be expected with the initial inclusion of Si from the activator. With increased curing time, the Ca/Si ratio shifts towards lower values, caused by the slower dissolution of Si and delayed incorporation of Si in C–A–S–H gels. For both curing times the EDX points are quite clustered together, meaning high consistency in the binder phase.

EDX points describing 50C have a wider spread in their distribution, due to the higher complexity of the system. An increase in both Ca/Si and $(Al + Fe)/Si$ ratios could be possibly identified. This could be due to a delayed incorporation of Fe which is slowly released by CS. 100C shows minimal change in elemental composition with increase curing time. A minor shift could be identified from raw CS towards lower values of $(Al + Fe)/Si$ ratio, as the Si from the activator becomes included in the gel, followed by a small growth after 28 days, which might be due to subsequent incorporation of Al and Fe.

Mercury intrusion porosimetry

Figure 11 illustrates the pore size distributions of the mixtures after 2 and 28 days of curing. The pore sizes

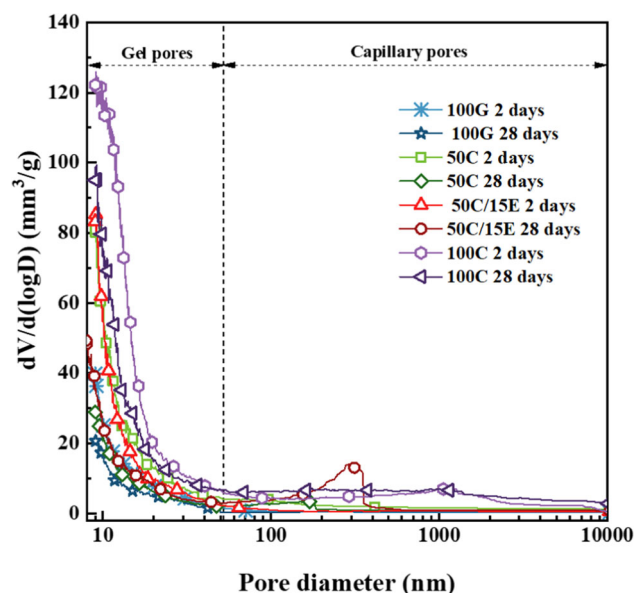


Figure 11 Differential porosity of alkali-activated specimens based on GGBFS, CS and EAFSS after 2 and 28 days of curing.

of alkali-activated mixtures can be classified as follows: gel pores in the range of 10 to 50 nm, capillary pores between 50 nm and 10 μm , and air voids (which were the pores visible by SEM in Sect. “Scanning electron microscopy”) over 10 μm [81]. The dominant type of porosity appears to be in the gel pore range for all alkali-activated mixtures. Almost no capillary pores are detected, except for sample 50C/15E after 28 days, which exhibits a limited amount of pores ~ 300 nm in size, and 100C with a regular distribution of pores between 50 nm and 1 μm .

The total porosities of the alkali-activated mixtures calculated from MIP data are given in Table 4. For all specimens, the total porosity decreases as the curing age continues. This is indicative of densification of the specimens through a gradual reduction of gel pores as new gel phases form [25, 82–84].

The inclusion of CS results in an initial increase in total porosity after 2 days, as seen for 50C when compared to 100G. After 28 days, the total porosity of 50C is reduced by more than 50%. The inclusion of EAFSS appears to be initially beneficial in reducing initial porosity, most likely due to improved particle packing from the differences in precursor particle size distributions [85]. After 28 days the reduction in total porosity of 50C/15E is minimal, this is because despite the reduction in gel porosity, a new type of pores has formed in the macropore region, as shown in Fig. 11, denoting a lower degree of structural evolution. This is also associated with the increased content of stable mineral phases in the EAFSS that do not take part in any pore-filling reaction [24, 25, 82]. Mix 100C has the highest total porosity, and very little reduction ($\sim 2\%$) is obtained with increasing curing times.

The increase in porosity when replacing GGBFS by other less-reactive slags may also depend on the

nature of the gel type [86]. Each individual type of binding gel promotes a distinctive pore structure [87], specifically the main reaction product of GGBFS is C–A–S–H gel, whereas alkali-activated CS forms a low-calcium iron-rich aluminosilicate gel [32] which may not be as dense as conventional C–A–S–H gels [88].

Strength properties

Figure 12 shows the compressive and flexural strengths developed by alkali-activated mortars after 1, 3, 7 and 28 days. Replacing GGBFS with CS and EAFSS resulted in an overall reduction of compressive and flexural strength, depending on the degree of replacement. This apparent strength loss is more noticeable when comparing the 1-day specimens, with the difference between 100G and 50C being a reduction by approximately 50%. This effect has been generally explained in the previous sections by the limited structural evolution and slower kinetics/reactivity of CS and EAFSS, compared to GGBFS, during alkali activation. From the calorimetry data discussed previously (Fig. 3), the greater release of heat for the 100G mixture at early ages compared to CS mixtures suggests a more rapid degree of polycondensation and formation of strength-giving phases, hence the large difference in strength properties. The difference in mechanical properties between specimens 100G and 50C becomes minor at later ages, with only a 9% strength loss in compression and 14% loss in flexural strength after 28 days of curing even at the high degree of GGBFS replacement used in 50C, suggesting that binders of comparable quality can be produced with 50% (or maybe further) replacement of GGBFS by alternative slags.

It is interesting to note that between the ternary samples, 50C/35E has the highest 1-day strength, but it reaches the lowest 28-day strength. This can be the result of the high amount of available activator for GGBFS to promptly and fully react during the early stages, followed by a deceleration of the reaction, leading to a lower eventual strength development. This is in agreement with the calorimetry data, and the behaviour is typically seen for filler materials of small particle size as EAFSS which allow high availability of activator in the system and additional surface area for the nucleation of hydration products at early ages [89]. Although reaching the lowest strength values among the blended binders after 28 days, 50C/35E still passes 50 MPa in compression

Table 4 Total porosity of alkali-activated pastes, measured by MIP after 2 and 28 days of curing

Mixture	Total porosity (vol. %)	
	2 days	28 days
100 G	2.55	1.75
50C	5.95	2.80
50C/15E	4.95	4.00
100C	10.90	9.00

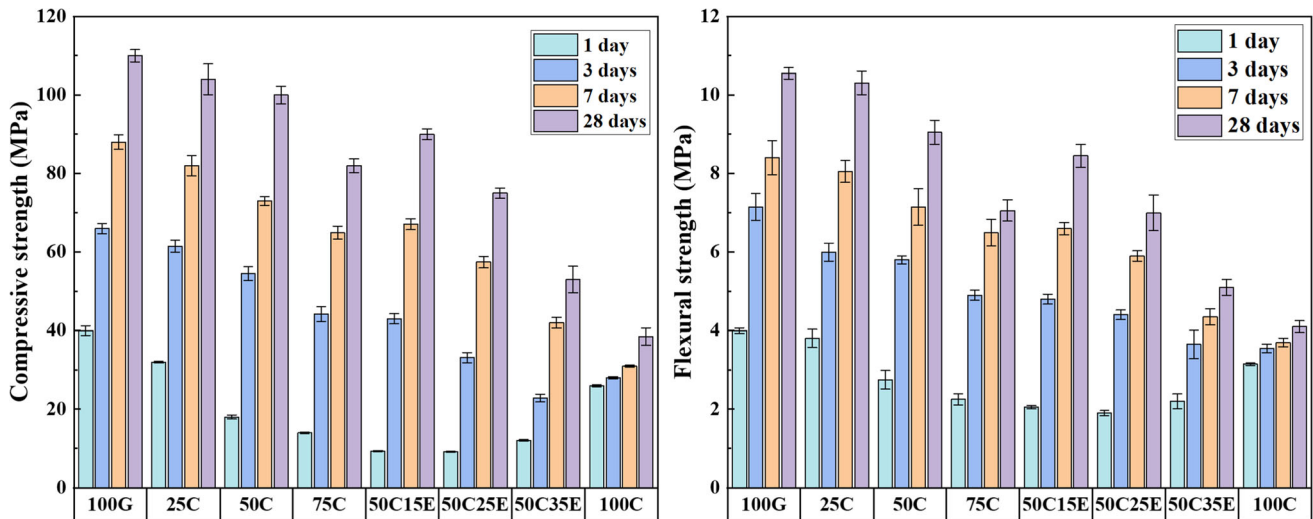


Figure 12 Compressive and flexural strength of alkali-activated mortars based on GGBFS, CS and EAFSS after 1, 3, 7 and 28 days.

and 5 MPa in bending, meaning that it has more than sufficient strength for a wide range of potential practical applications.

The 100C sample shows a remarkable early-age compressive strength of over 20 MPa after 1 day, arising from the formation of strength phases during the first 24 h. This result agrees with the exothermic peak developed within 24 h of reaction seen in the calorimetry data (Fig. 3), which is believed to be due to both dissolution of the precursors in an activator-rich environment, and the generation of a binding phase composed primarily of $\text{CaO-FeO}_x\text{-Al}_2\text{O}_3\text{-SiO}_2$ derived from the elements present in the CS. In contrast to GGBFS-based mixtures, the increase in strength after 1 day is near-negligible. This is likely due to the low continuing availability of calcium, resulting in limited C–S–H/C–A–S–H gel formation [90]. Similar findings were reported by Siakati et al. [90], where mixtures at low CaO/FeO molar ratios exhibited a larger extent of reactivity at early age, followed by minimal improvements of mechanical strength over time. Increasing the CaO/FeO ratio was found to inhibit reactivity at early ages, while further improving late age properties through the incorporation of Ca into an iron phyllosilicate-type structure.

All AAMs investigated are consistent with the compressive strength requirement of the 52.5 N cement strength class according to EN 197–1, except for 100C and 50C35E. Previous studies have shown that alkali activation of CS with NaOH leads to very low compressive strength values (< 5 MPa) [15, 91]. In contrast, when considering blends of 70 wt. % CS

with 30 wt. % metakaolin or fly ash activated with a sodium silicate solution of similar alkali dosage to that used in the present study, compressive strength of approximately 30 MPa and 40 MPa were achieved after 28 days [33]. These findings indicate that blending CS with GGBFS yields a more efficient binder, as demonstrated by 75C reaching over 80 MPa after 28 days. Another observation from the same study [33] was that the compressive strength of 100 wt. % CS fell within the same range of approximately 30 MPa after 28 days.

Leaching tests

Leaching of heavy metals from monolithic specimens was evaluated through ICP analysis of leachates, and the results for samples 100G, 50C and 50C/15E are presented in Table 5. The leaching values for each element are calculated following NEN-7345:94 and each element is categorised as follows: class C1 if the leaching potential of all hazardous elements is below the threshold value specified as U1; class C2 if the leaching value of one or more hazardous elements falls between the threshold values specified as U1 and U2; and class C3 when the leaching of any element is above the limit U2. The tests have been performed on paste being part of concrete as a building product. Because U-references applicable to paste do not exist, in Table 5 reference is made to U-references for building products according to NEN-7345.

Sample 100G can be classified as C1 as all of the leaching values obtained are below the U1 limits,

Table 5 Results obtained from ICP and calculated following NEN-7345:94 test [59] for samples 100G and 50C, and 50C/50E, and comparison with limits U1 and U2, where problematic results are underlined

Sample (mg/m ²)	As	Ba	Cd	Co	Cr	Cu	Hg	Mo	Ni	Pb	Sb	Se	V	Zn
100G	< 0.5	3.3	< 0.1	0.2	< 0.2	< 0.2	< 0.3	< 0.2	2.3	< 0.5	< 0.8	< 1.2	0.2	1.1
50C	< 0.5	0.8	< 0.1	1.3	0.7	<u>57.6</u>	< 0.3	<u>120.6</u>	2.7	< 0.5	< 0.8	< 1.2	0.4	109.4
50C/15E	< 0.5	0.3	< 0.1	1.4	0.7	<u>62.2</u>	< 0.3	<u>131.1</u>	4.2	< 0.5	< 0.8	< 1.2	1.5	89.3
U1	40	600	1	25	150	50	0.4	15	50	100	3.5	3	250	200
U2	300	45,000	7.5	200	950	350	3	95	350	800	25	20	1500	1500

meaning that there are no environmental restrictions in the usage of this mixture according to NEN-7345. However, both samples 50C and 50C/15E, containing 50 wt.% CS, have two problematic elements: Cu which in both cases falls into class C2 and Mo which is above the U2 limit and thus places the material into C3, meaning that these binders can have only limited utilisation as construction materials. From previous studies [92] we can deduce that both Cu and Mo are leaching from CS only. Comparing the two binders it can be observed that a higher amount of hazardous elements is immobilised for higher contents of GGBFS, e.g. sample 50G over 50G/15E. It is possible to assume that a modest reduction of CS content in a mixture, in favour of GGBFS, would generate a binder which complies with the standard values by falling within classes C1 or C2. This is also due to the highly reducing environment provided by the sulphide content in GGBFS, known to be beneficial in the reduction of leaching of redox-sensitive transition metals [93]. Note, however, that a different outcome might be obtained from studies at a concrete level due to the dilution effect of the aggregates versus paste only. The results here should thus be considered with care in this respect.

Conclusions

In this study, the properties of alkali-activated pastes based on CS and EAFSS as partial and total replacements for GGBFS have been investigated.

The findings show that alkali activation of solely CS-based and GGBFS-based mixes results in contrasting calorimetry profiles. Alkali-activated CS exhibits a broad intense heat release peak followed by negligible heat evolution increase, whilst GGBFS-

based samples exhibit dissolution and reaction peaks. CS addition result in increased dormant periods and reduced peak intensities. EAFSS acts as a filler, enhancing activator availability per unit mass and reducing dormant periods of ternary mixtures. Both workability and setting times increase with replacement of GGBFS due to the better retention of workability properties promoted by the low early reactivity and dissolution of CS particles, and the stability of mineral phases of EAFSS. XRD analysis reveals that alkali activation of GGBFS generates C–A–S–H gel, disordered hydrotalcite and calcite, whilst increasing CS replacements their formation is reduced and not detectable for 100 wt. % CS paste in which the calcium content is too low. The crystalline phases of CS and EAFSS remain stable throughout alkali activation. FTIR spectra of CS-based samples indicate shifts that may be related to the oxidation of Fe²⁺ to Fe³⁺. All samples show increased incorporation of Al³⁺ or Fe³⁺ over time, except 100% CS which shows minimal change between 2- and 28-day spectra. SEM analysis reveals matrix densification over time, except for alkali-activated 100 wt. % CS. Total porosity initially increases with 50 wt. % CS addition, but after 28 days, the difference from 100 wt. % GGBFS-AAM is minimal. Ternary blends with CS and EAFSS have lower initial porosity than binary blends due to improved particle packing, but develop macroporosity after 28 days due to coarse crystalline phases. Mechanical properties decrease when replacing GGBFS with CS, but the difference diminishes with time. After 28 days, compressive and flexural strength values reach 53 MPa and 5.1 MPa for a sample based on only 15 wt. % GGBFS in a ternary blend, and 38 MPa and 4.10 MPa for 100 wt. % CS, suggesting that CS is a potential alternative precursor to GGBFS. Leaching tests identify Cu and

Mo as problematic elements associated with CS use, potentially limiting GGBFS replacement levels by CS.

Overall, CS can be a suitable precursor in alkali activation and replacement for GGBFS, whereas EAFSS has proved to be an adequate filler material. The proven reactivity of CS in alkali activation, as seen in this work and other reported studies on CS, provide a foundation for CS to be utilised as a more sustainable alternative to traditional binders. This study considered the fresh, microstructural and strength properties of CS and ternary binders. Further work is required to characterise other important properties such as durability and late age performance, along with additional investigation on the effects of leaching in mortars and concretes containing CS. This is necessary to ascertain a maximum CS inclusion level that avoids significant leaching of Mo and Cu that would limit the application of CS. The outcomes of this research may further guide sustainable construction practices.

Acknowledgements

This research study was carried out in the framework of the “By-products for sustainable concrete in the urban environment” (URBCON) project-NWE 725, funded by the Interreg North-West Europe Programme under the EU Cohesion Policy and financed by the European Regional Development Fund (ERDF). Additionally, the authors wish to express their gratitude towards Ecocem, Aurubis and Orbix for providing the slags used in this study.

Open Access This article is licensed under a Creative Commons Attribution 4.0 International License, which permits use, sharing, adaptation, distribution and reproduction in any medium or format, as long as you give appropriate credit to the original author(s) and the source, provide a link to the Creative Commons licence, and indicate if changes were made. The images or other third party material in this article are included in the article’s Creative Commons licence, unless indicated otherwise in a credit line to the material. If material is not included in the article’s Creative Commons licence and your intended use is not permitted by statutory regulation or exceeds the permitted use, you will need to obtain permission directly from the copyright

holder. To view a copy of this licence, visit <http://creativecommons.org/licenses/by/4.0/>.

References

- [1] Gencil O, Karadag O, Oren OH, Bilir T (2021) Steel slag and its applications in cement and concrete technology: a review. *Constr Build Mater* 283:122783. <https://doi.org/10.1016/j.conbuildmat.2021.122783>
- [2] Rodrigues FA, Joekes I (2011) Cement industry: sustainability, challenges and perspectives. *Environ Chem Lett* 9(2):151–166. <https://doi.org/10.1007/s10311-010-0302-2>
- [3] Phiri TC, Singh P, Nikoloski AN (2021) The potential for copper slag waste as a resource for a circular economy: a review – Part II*. *Miner Eng* 172:107150. <https://doi.org/10.1016/j.mineng.2021.107150>
- [4] Benachio GLF, Freitas MDCD, Tavares SF (2020) Circular economy in the construction industry: a systematic literature review. *J Clean Prod* 260:121046. <https://doi.org/10.1016/j.jclepro.2020.121046>
- [5] Ndahirwa D, Zmamou H, Lenormand H, Leblanc N (2022) The role of supplementary cementitious materials in hydration, durability and shrinkage of cement-based materials, their environmental and economic benefits: a review. *Clean Mater* 5:100123. <https://doi.org/10.1016/j.clema.2022.100123>
- [6] Shah IH, Miller SA, Jiang D, Myers RJ (2022) Cement substitution with secondary materials can reduce annual global CO₂ emissions by up to 1.3 gigatons. *Nat Commun* 13(1):1–11. <https://doi.org/10.1038/s41467-022-33289-7>
- [7] Oliver JGJ, Janssens-Maenhout G, Muntean M, Peters JAHW (2016) Trends in global CO₂ emissions. PBL Publishers, The Hague
- [8] Provis JL, Palomo A, Shi C (2015) Advances in understanding alkali-activated materials. *Cem Concr Res* 78:110–125. <https://doi.org/10.1016/j.cemconres.2015.04.013>
- [9] Provis JL, Bernal SA (2014) Geopolymers and related alkali-activated materials. *Annu Rev Mater Res* 44(1):299–327. <https://doi.org/10.1146/annurev-matsci-070813-113515>
- [10] Shi C, Fernández Jiménez A, Palomo A (2011) New cements for the 21st century: The pursuit of an alternative to Portland cement. *Cem Concr Res* 41(7):750–763. <https://doi.org/10.1016/j.cemconres.2011.03.016>
- [11] Ding Y, Dai J-G, Shi C-J (2016) Mechanical properties of alkali-activated concrete: a state-of-the-art review. *Constr Build Mater* 127:68–79. <https://doi.org/10.1016/j.conbuildmat.2016.09.121>

- [12] Bernal SA, Provis JL (2014) Durability of alkali-activated materials: progress and perspectives. *J Am Ceram Soc* 100(8):997–1008. <https://doi.org/10.1111/jace.12831>
- [13] Shi C, Roy D, Krivenko P (2006) *Alkali-Activated Cements and Concretes*. Taylor & Francis, London
- [14] Juenger MCG, Snellings R, Bernal SA (2019) Supplementary cementitious materials: new sources, characterization, and performance insights. *Cem Concr Res* 122:257–273. <https://doi.org/10.1016/j.cemconres.2019.05.008>
- [15] Yan Z, Sun Z, Yang J, Yang H, Ji Y, Hu K (2021) Mechanical performance and reaction mechanism of copper slag activated with sodium silicate or sodium hydroxide. *Constr Build Mater* 266:120900. <https://doi.org/10.1016/j.conbuildmat.2020.120900>
- [16] Gómez-Casero MA, Pérez-Villarejo L, Sánchez-Soto PJ, Eliche-Quesada D (2022) Comparative study of alkali activated cements based on metallurgical slags, in terms of technological properties developed. *Sustain Chem Pharm* 29:100746. <https://doi.org/10.1016/j.scp.2022.100746>
- [17] Gorai B, Jana RK, Premchand, (2003) Characteristics and utilisation of copper slag—a review. *Resour Conserv Recycl* 39(4):299–313. [https://doi.org/10.1016/S0921-3449\(02\)00171-4](https://doi.org/10.1016/S0921-3449(02)00171-4)
- [18] Huaiwei Z, Xin H (2011) An overview for the utilization of wastes from stainless steel industries. *Resour Conserv Recycl* 55(8):745–754. <https://doi.org/10.1016/j.resconrec.2011.03.005>
- [19] Lancellotti I, Piccolo F, Traven K, Češnovar M, Ducman V, Leonelli C (2021) Alkali activation of metallurgical slags: Reactivity, chemical behavior, and environmental assessment. *Materials (Basel)* 14(3):639. <https://doi.org/10.3390/ma14030639>
- [20] Özalp F (2022) Effects of electric arc furnace (EAF) slags on mechanical and permeability properties of paving stone, kerb and concrete pipes. *Constr Build Mater* 329:127159. <https://doi.org/10.1016/j.conbuildmat.2022.127159>
- [21] Lizasoain-Arteaga E, Lastra-González P, Indacochea-Vega I, Flintsch G (2020) Comprehensive analysis of the environmental impact of electric arc furnace steel slag on asphalt mixtures. *J Clean Prod* 275:123121. <https://doi.org/10.1016/j.jclepro.2020.123121>
- [22] Monosi S, Ruello ML, Sani D (2016) Electric arc furnace slag as natural aggregate replacement in concrete production. *Cem Concr Compos* 66:66–72. <https://doi.org/10.1016/j.cemconcomp.2015.10.004>
- [23] Keymanesh MR, Ziari H, Zalnezhad H, Zalnezhad M (2021) Mix design and performance evaluation of microsurfacing containing electric arc furnace (EAF) steel slag filler. *Constr Build Mater* 269:121336. <https://doi.org/10.1016/j.conbuildmat.2020.121336>
- [24] Furlani E et al (2018) Synthesis and characterization of geopolymers containing blends of unprocessed steel slag and metakaolin: The role of slag particle size. *Ceram Int* 44(5):5226–5232. <https://doi.org/10.1016/j.ceramint.2017.12.131>
- [25] Song W et al (2019) Effect of steel slag on fresh, hardened and microstructural properties of high-calcium fly ash based geopolymers at standard curing condition. *Constr Build Mater* 229:116933. <https://doi.org/10.1016/j.conbuildmat.2019.116933>
- [26] Song W et al (2020) Efficient use of steel slag in alkali-activated fly ash-steel slag-ground granulated blast furnace slag ternary blends. *Constr Build Mater* 259:119814. <https://doi.org/10.1016/j.conbuildmat.2020.119814>
- [27] Edwin RS, Gruyaert E, De Belie N (2022) Valorization of secondary copper slag as aggregate and cement replacement in ultra-high performance concrete. *J Build Eng* 54:104567. <https://doi.org/10.1016/j.jobe.2022.104567>
- [28] Mithun BM, Narasimhan MC (2016) Performance of alkali activated slag concrete mixes incorporating copper slag as fine aggregate. *J Clean Prod* 112:837–844. <https://doi.org/10.1016/j.jclepro.2015.06.026>
- [29] Shi C, Meyer C, Behnood A (2008) Utilization of copper slag in cement and concrete. *Resour Conserv Recycl* 52(10):1115–1120. <https://doi.org/10.1016/j.resconrec.2008.06.008>
- [30] Kuterasińska J, Król A (2015) Mechanical properties of alkali-activated binders based on copper slag. *Archit Civ Eng Environ* 8:61–67
- [31] Nazer A, Payá J, Borrachero MV, Monzó J (2016) Use of ancient copper slags in Portland cement and alkali activated cement matrices. *J Environ Manage* 167:115–123. <https://doi.org/10.1016/j.jenvman.2015.11.024>
- [32] Peys A, Douvalis AP, Hallet V, Rahier H, Blanpain B, Pontikes Y (2019) Inorganic polymers from CaO-FeO_x-SiO₂ slag: the start of oxidation of Fe and the formation of a mixed valence binder. *Front Mater* 6(212):1–10
- [33] Singh J, Singh SP (2019) Development of alkali-activated cementitious material using copper slag. *Constr Build Mater* 211:73–79. <https://doi.org/10.1016/j.conbuildmat.2019.03.233>
- [34] Ahmari S, Parameswaran K, Zhang L (2015) Alkali activation of copper mine tailings and low-calcium flash-furnace copper smelter slag. *J Mater Civ Eng* 27:6. [https://doi.org/10.1061/\(ASCE\)MT.1943-5533.0001159](https://doi.org/10.1061/(ASCE)MT.1943-5533.0001159)
- [35] Dhir RK, de Brito J, Mangabhai R, Lye CQ (2016) *Sustainable Construction Materials - Copper Slag*. Woodhead Publishing, Abingdon
- [36] Piatak NM, Parsons MB, Seal RR (2015) Characteristics and environmental aspects of slag: a review. *Appl Geochem*

- 57:236–266. <https://doi.org/10.1016/j.apgeochem.2014.04.009>
- [37] Pontikes Y et al (2013) Slags with a high Al and Fe content as precursors for inorganic polymers. *Appl Clay Sci* 73:93–102. <https://doi.org/10.1016/j.clay.2012.09.020>
- [38] Siakati C et al (2020) Unraveling the nano-structure of a glassy CaO-FeO-SiO₂ slag by molecular dynamics simulations. *J Non Cryst Solids* 528:119771. <https://doi.org/10.1016/j.jnoncrsol.2019.119771>
- [39] Adedirani A, Yliniemi J, Illikainen M (2021) Development of sustainable alkali-activated mortars using Fe-rich fayalitic slag as the sole solid precursor. *Front Built Environ* 7:653466. <https://doi.org/10.3389/fbuil.2021.653466>
- [40] Siakati C, Douvalis AP, Ziogas P, Peys A, Pontikes Y (2020) Impact of the solidification path of FeO_x-SiO₂ slags on the resultant inorganic polymers. *J Am Ceram Soc* 103(3):2173–2184. <https://doi.org/10.1111/jace.16869>
- [41] Monich PR, Romero AR, Höllen D, Bernardo E (2018) Porous glass-ceramics from alkali activation and sinter-crystallization of mixtures of waste glass and residues from plasma processing of municipal solid waste. *J Clean Prod* 188:871–878. <https://doi.org/10.1016/j.jclepro.2018.03.167>
- [42] Kalinkin AM et al (2012) Geopolymerization behavior of Cu – Ni slag mechanically activated in air and in CO₂ atmosphere. *Int J Miner Process* 112–113:101–106. <https://doi.org/10.1016/j.minpro.2012.05.001>
- [43] Komnitsas K, Zaharaki D, Perdikatsis V (2007) Geopolymerisation of low calcium ferronickel slags. *J Mater Sci* 42(9):3073–3082. <https://doi.org/10.1007/s10853-006-0529-2>
- [44] Teo PT et al (2020) Assessment of electric arc furnace (EAF) steel slag waste's recycling options into value added green products: A review. *Metals (Basel)* 10(10):1347. <https://doi.org/10.3390/met10101347>
- [45] Fan Y, Zhang B, Song J, Volski V, Vandenbosch G, Guo M (2018) An innovated application of reutilize copper smelter slag for cement-based electromagnetic interference composites. *Sci Rep* 8(1):16155. <https://doi.org/10.1038/s41598-018-34680-5>
- [46] Menad N-E, Kana N, Seron A, Kanari N (2021) New EAF slag characterization methodology for strategic metal recovery. *Materials (Basel)* 14:6. <https://doi.org/10.3390/ma14061513>
- [47] Zhang S et al (2021) A novel strategy for harmlessness and reduction of copper smelting slags by alkali disaggregation of fayalite (Fe₂SiO₄) coupling with acid leaching. *J Hazard Mater* 402:123791. <https://doi.org/10.1016/j.jhazmat.2020.123791>
- [48] Lee WKW, van Deventer JSJ (2003) Use of infrared spectroscopy to study geopolymerization of heterogeneous amorphous aluminosilicates. *Langmuir* 19(21):8726–8734. <https://doi.org/10.1021/la026127e>
- [49] Peys A, White CE, Olds D, Rahier H, Blanpain B, Pontikes Y (2018) Molecular structure of CaO-FeO_x-SiO₂ glassy slags and resultant inorganic polymer binders. *J Am Ceram Soc* 101(12):5846–5857. <https://doi.org/10.1111/jace.15880>
- [50] Dalby KN, King PL (2006) A new approach to determine and quantify structural units in silicate glasses using micro-reflectance Fourier-transform infrared spectroscopy. *Am Mineral* 91(11–12):1783–1793. <https://doi.org/10.2138/am.2006.2075>
- [51] Addadi L, Raz S, Weiner S (2003) Taking advantage of disorder: amorphous calcium carbonate and its roles in biomineralization. *Adv Mater* 15(12):959–970. <https://doi.org/10.1002/adma.200300381>
- [52] Stefanescu M, Barbu M, Vlase T, Barvinschi P, Barbu-Tudoran L, Stoia M (2011) Novel low temperature synthesis method for nanocrystalline zinc and magnesium chromites. *Thermochim Acta* 526(1):130–136. <https://doi.org/10.1016/j.tca.2011.09.005>
- [53] Kalinkina EV, Kalinkin AM, Forsling W, Makarov VN (2001) Sorption of atmospheric carbon dioxide and structural change of Ca and Mg silicate minerals during grinding II. Enstatite, åkermanite and wollastonite. *Int J Miner Process* 61(4):289–299. [https://doi.org/10.1016/S0301-7516\(00\)00038-7](https://doi.org/10.1016/S0301-7516(00)00038-7)
- [54] British Standards Institution, (2016) BS EN 196–3:2016 Methods of testing cement - Part 3: Determination of setting times and soundness.
- [55] Wadsö L (2010) Operational issues in isothermal calorimetry. *Cem Concr Res* 40(7):1129–1137. <https://doi.org/10.1016/j.cemconres.2010.03.017>
- [56] Tan Z, Bernal SA, Provis JL (2017) Reproducible mini-slump test procedure for measuring the yield stress of cementitious pastes. *Mater Struct* 50(6):1–12. <https://doi.org/10.1617/s11527-017-1103-x>
- [57] Zeng Q, Li K, Fen-Chong T, Dangla P (2012) Analysis of pore structure, contact angle and pore entrapment of blended cement pastes from mercury porosimetry data. *Cem Concr Compos* 34(9):1053–1060. <https://doi.org/10.1016/j.cemconcomp.2012.06.005>
- [58] British Standards Institution (2019) BS EN 1015–11:2019, Methods of test for mortar for masonry - Determination of flexural and compressive strength of hardened mortar
- [59] Nederlands Normalisatie-Instituut (1994) NEN-7345:94 Leaching characteristics of solid earthy and stony building and waste materials - Leaching tests - Determination of the leaching of inorganic components from buildings and monolithic waste materials with the diffusion test

- [60] Zuo Y, Ye G (2020) Preliminary interpretation of the induction period in hydration of sodium hydroxide/silicate activated slag. *Materials* (Basel) 13(21):4796. <https://doi.org/10.3390/ma13214796>
- [61] Bernal SA, San Nicolas R, van Deventer JSJ, Provis JL (2016) Alkali-activated slag cements produced with a blended sodium carbonate/sodium silicate activator. *Adv Cem Res* 28(4):262–273. <https://doi.org/10.1680/jadcr.15.00013>
- [62] Ben Haha M, Lothenbach B, Le Saout G, Winnefeld F (2011) Influence of slag chemistry on the hydration of alkali-activated blast-furnace slag — Part I: effect of MgO. *Cem Concr Res* 41(9):955–963. <https://doi.org/10.1016/j.cemconres.2011.05.002>
- [63] You N, Li B, Cao R, Shi J, Chen C, Zhang Y (2019) The influence of steel slag and ferronickel slag on the properties of alkali-activated slag mortar. *Constr Build Mater* 227:116614. <https://doi.org/10.1016/j.conbuildmat.2019.07.340>
- [64] Fernández-Jiménez A, Puertas F (2003) Effect of activator mix on the hydration and strength behaviour of alkali-activated slag cements. *Adv Cem Res* 15(3):126–136. <https://doi.org/10.1680/adcr.13.3.115.39288>
- [65] Wang S-D, Scrivener KL (1995) Hydration products of alkali activated slag cement. *Cem Concr Res* 25(3):561–571. [https://doi.org/10.1016/0008-8846\(95\)00045-E](https://doi.org/10.1016/0008-8846(95)00045-E)
- [66] Walkley B et al (2016) Phase evolution of C-(N)-A-S-H/N-A-S-H gel blends investigated via alkali-activation of synthetic calcium aluminosilicate precursors. *Cem Concr Res* 89:120–135
- [67] Bernal SA et al (2013) Gel nanostructure in alkali-activated binders based on slag and fly ash, and effects of accelerated carbonation. *Cem Concr Res* 53:127–144. <https://doi.org/10.1016/j.cemconres.2013.06.007>
- [68] Richardson IG, Brough AR, Groves GW, Dobson CM (1994) The characterization of hardened alkali-activated blast-furnace slag pastes and the nature of the calcium silicate hydrate (C-S-H) phase. *Cem Concr Res* 24(5):813–829. [https://doi.org/10.1016/0008-8846\(94\)90002-7](https://doi.org/10.1016/0008-8846(94)90002-7)
- [69] Ye H, Radlińska A (2017) Carbonation-induced volume change in alkali-activated slag. *Constr Build Mater* 144:635–644. <https://doi.org/10.1016/j.conbuildmat.2017.03.238>
- [70] A. Adediran, J. Yliniemi, and M. Illikainen, (2019) “Fayalite slag as binder and aggregate in alkali-activated materials—interfacial transition zone study,” In: *Proceedings of 1st International Conference on Smart Materials for Sustainable Construction—SMASCO 2019*. Luleå, doi: <https://doi.org/10.3390/proceedings2019034001>.
- [71] Nikolov A (2020) Alkali and acid activated geopolymers based on iron-silicate fines - by-product from copper industry. *Mach Technol Mater* 14(1):37–39
- [72] Yu P, Kirkpatrick RJ, Poe B, McMillan PF, Cong X (1999) Structure of calcium silicate hydrate (C-S-H): near-, mid-, and far-infrared spectroscopy. *J Am Ceram Soc* 82(3):742–748. <https://doi.org/10.1111/j.1151-2916.1999.tb01826.x>
- [73] Puertas F, Palacios M, Vázquez T (2006) Carbonation process of alkali-activated slag mortars. *J Mater Sci* 41(10):3071–3082. <https://doi.org/10.1007/s10853-005-1821-2>
- [74] Li N, Farzadnia N, Shi C (2017) Microstructural changes in alkali-activated slag mortars induced by accelerated carbonation. *Cem Concr Res* 100:214–226. <https://doi.org/10.1016/j.cemconres.2017.07.008>
- [75] Criado M, Fernández-Jiménez A, Palomo A (2007) Alkali activation of fly ash: Effect of the SiO₂/Na₂O ratio: Part I: FTIR study. *Micropor Mesopor Mater* 106(1):180–191. <https://doi.org/10.1016/j.micromeso.2007.02.055>
- [76] Hajimohammadi A, Provis JL, Van Deventer JSJ (2010) Effect of alumina release rate on the mechanism of geopolymer gel formation. *Chem Mater* 22(18):5199–5208. <https://doi.org/10.1021/cm101151n>
- [77] Fernández-Jiménez A, Palomo A (2005) Mid-infrared spectroscopic studies of alkali-activated fly ash structure. *Micropor Mesopor Mater* 86(1–3):207–214. <https://doi.org/10.1016/j.micromeso.2005.05.057>
- [78] Onisei S, Douvalis AP, Malfliet A, Peys A, Pontikes Y (2018) Inorganic polymers made of fayalite slag: on the microstructure and behavior of Fe. *J Am Ceram Soc* 101(6):2245–2257. <https://doi.org/10.1111/jace.15420>
- [79] Peys A, White CE, Rahier H, Blanpain B, Pontikes Y (2019) Alkali-activation of CaO-FeO_x-SiO₂ slag: formation mechanism from in-situ X-ray total scattering. *Cem Concr Res* 122:179–188. <https://doi.org/10.1016/j.cemconres.2019.04.019>
- [80] Hasan MM, Rhamdhani MA, Shuva MAH, Brooks GA (2020) Study of the structure of FeO_x-CaO-SiO₂-MgO and FeO_x-CaO-SiO₂-MgO-Cu₂O-PdO slags relevant to urban ores processing through Cu smelting. *Metals* (Basel) 10(1):8. <https://doi.org/10.3390/met10010078>
- [81] Ma Y, Hu J, Ye G (2013) The pore structure and permeability of alkali activated fly ash. *Fuel* 104:771–780. <https://doi.org/10.1016/j.fuel.2012.05.034>
- [82] Cao R, Li B, You N, Zhang Y, Zhang Z (2018) Properties of alkali-activated ground granulated blast furnace slag blended with ferronickel slag. *Constr Build Mater* 192:123–132. <https://doi.org/10.1016/j.conbuildmat.2018.10.112>

- [83] Sindhunata, Van Deventer JSJ, Lukey GC, Xu H (2006) Effect of curing temperature and silicate concentration on fly-ash-based geopolymerization. *Ind Eng Chem Res* 45(10):3559–3568. <https://doi.org/10.1021/ie051251p>
- [84] Gao K et al (2014) Effects SiO₂/Na₂O molar ratio on mechanical properties and the microstructure of nano-SiO₂ metakaolin-based geopolymers. *Constr Build Mater* 53:503–510. <https://doi.org/10.1016/j.conbuildmat.2013.12.003>
- [85] Bondar D, Nanukuttan S, Provis JL, Soutsos M (2019) Efficient mix design of alkali activated slag concretes based on packing fraction of ingredients and paste thickness. *J Clean Prod* 218:438–449. <https://doi.org/10.1016/j.jclepro.2019.01.332>
- [86] Ismail I, Bernal SA, Provis JL, San Nicolas R, Hamdan S, van Deventer JSJ (2014) Modification of phase evolution in alkali-activated blast furnace slag by the incorporation of fly ash. *Cem Concr Compos* 45:125–135. <https://doi.org/10.1016/j.cemconcomp.2013.09.006>
- [87] Provis JL, Myers RJ, White CE, Rose V, van Deventer JSJ (2012) X-ray microtomography shows pore structure and tortuosity in alkali-activated binders. *Cem Concr Res* 42(6):855–864. <https://doi.org/10.1016/j.cemconres.2012.03.004>
- [88] Walkley B, Ke X, Hussein O, Provis JL (2021) Thermodynamic properties of sodium aluminosilicate hydrate (N-A-S-H). *Dalton Trans* 50(39):13968–13984. <https://doi.org/10.1039/d1dt02202d>
- [89] Oey T, Kumar A, Bullard JW, Neithalath N, Sant G (2013) The filler effect: The influence of filler content and surface area on cementitious reaction rates. *J Am Ceram Soc* 96(6):1978–1990. <https://doi.org/10.1111/jace.12264>
- [90] Siakati C, Douvalis AP, Hallet V, Peys A, Pontikes Y (2021) Influence of CaO/FeO ratio on the formation mechanism and properties of alkali-activated Fe-rich slags. *Cem Concr Res* 146:106466. <https://doi.org/10.1016/j.cemconres.2021.106466>
- [91] Ma Q et al (2018) Performance of copper slag contained mortars after exposure to elevated temperatures. *Constr Build Mater* 172:378–386. <https://doi.org/10.1016/j.conbuildmat.2018.03.261>
- [92] Ghorbani S et al (2023) Characterisation of alkali-activated stainless steel slag and blast-furnace slag cements. *Cem Concr Compos*. <https://doi.org/10.1016/j.cemconcomp.2023.105230>
- [93] Zhang J, Provis JL, Feng D, van Deventer JSJ (2008) The role of sulfide in the immobilization of Cr(VI) in fly ash geopolymers. *Cem Concr Res* 38(5):681–688. <https://doi.org/10.1016/j.cemconres.2008.01.006>

Publisher's Note Springer Nature remains neutral with regard to jurisdictional claims in published maps and institutional affiliations.